KSME

Springer

Journal of Mechanical Science and Technology 38 (2) 2024

Original Article
DOI 10.1007/s12206-024-0145-6

Keywords:
· Capillary rate of rise
· Flexible
· Hierarchical structure
· Laser-induced graphene
· Porous graphene
· Thermal management

Correspondence to:
Hyoungsoon Lee
leeh@cau.ac.kr

Citation:
Kang, M., Kong, D., Park, J., In, J. B., Lee, H. (2024). Enhanced wick-based liquid supply in patterned laser-induced graphene on flexible substrates. Journal of Mechanical Science and Technology 38 (2) (2024) ?~?.
http://doi.org/10.1007/s12206-024-0145-6

Received October 14th, 2023
Revised November 1st, 2023
Accepted November 13th, 2023

† Recommended by Editor Tong Seop Kim

© The Korean Society of Mechanical Engineers and Springer-Verlag GmbH Germany, part of Springer Nature 2024

Enhanced wick-based liquid supply in patterned laser-induced graphene on flexible substrates

Minsoo Kang[1], Daeyoung Kong[2,3], Junrae Park[1], Jung Bin In[1,3] and Hyoungsoon Lee[1,3]

[1]Department of Intelligent Energy and Industry, Chung-Ang University, Seoul 06974, Korea, [2]Department of Mechanical Engineering, Stanford University, Stanford, CA, 94305 USA, [3]School of Mechanical Engineering, Chung-Ang University, Seoul 06974, Korea

Abstract Advances in MEMS technology have enabled the development of smaller and more efficient electronic devices, integrating nanoscale components. Coupled with progress in flexible semiconductors, the potential applications of flexible electronics have significantly broadened. Yet, wearable and flexible electronics often face challenges related to thermal management owing to the low thermal conductivity of polymers--a crucial issue for wearables in direct contact with the skin. This study introduces an innovative approach to enhance wicking performance on flexible substrates aiming to improve thermal management. The approach involves creating intricate porous patterns on graphene structures through direct laser writing, using a CO_2 laser on a polyimide substrate with specific parameters. Eight distinct laser-induced graphene (LIG) samples were produced, each with different laser powers ranging from 9 to 23 W. A surface analysis confirmed the successful transformation of polyimide into porous graphene through laser ablation. The surface properties were evaluated before and after the oxygen plasma treatment, supported by XRD and XPS results. The liquid transport capacity of the LIG samples was accurately measured using the capillary rate-of-rise method. Lower powers (9 and 11 W) exhibited slower rates of wicking velocity, ranging from 5.0 mm/s$^{0.5}$ to 6.3 mm/s$^{0.5}$, whereas higher powers demonstrated increased rates, reaching 9.5 to 13.6 mm/s$^{0.5}$. These findings explicitly demonstrate the superior liquid delivery capability of LIG, achieving wicking velocities up to four times higher than those in relevant existing studies.

1. Introduction

Advancements in MEMS technology have led to producing small and high-performing electronic devices, integrating electronic components at the nanoscale. This, along with the significant advancements in flexible semiconductor technology, has vastly expanded the potential applications of flexible devices, including flexible displays, wearable electronics, biomedical implants, electronic skins, flexible solar cells, and foldable devices [1, 2]. Furthermore, the development of wireless communication technology for large-scale data transmission has spurred the innovation of technologies, such as IoT-based flexible and wearable devices that connect smartphones to IoT devices. Despite these advancements, the performance of wearable and flexible electronics is often hindered by thermal limitations, primarily owing to the use of inherently low thermal conductivity polymer materials for flexible printed circuit board substrates, such as polyethylene terephthalate, polyester, and polyimide (PI) [3-5]. This is particularly significant for wearable devices in direct contact with the skin and underscores the critical need for effective thermal management to reduce the risk of skin burns [6, 7].

Owing to the compact and lightweight nature of wearable devices, implementation of active cooling methods using fans or pumps is impossible. As an alternative, passive cooling methods, such as vapor chambers or heat pipes, which do not rely on external power sources, have become feasible. These techniques utilize porous structures to transport the working fluid to a hot spot where it evaporates and dissipates heat. Consequently, the cooling performance of these

techniques is significantly influenced by the wicking performance of porous structures. Hence, numerous studies have been conducted to create novel porous materials for enhancing wicking capabilities [8-12]. Xiao et al. developed a prediction model of liquid propagation rates in micropillar arrays and verified with experiments of deionized water (DI-water) in silicon micropillar arrays [8]. The sample wicked approximately 8 mm in 1 s. Using the Surface Evolver simulation program, they predicted the meniscus shape of the working fluid. The model showed agreement to within 5 % and design guidelines are provided. Yuan et al. chemically etched a copper substrate to create a hierarchical surface for capillary wicking [12]. The etched copper exhibited a nanograss and microflower shape, with 0° contact angle. The nanograss- and microflower-shaped copper substrate tested wicking velocity using droplet spreading measurement and showed 5.5 mm spreading in 0.5 s.

Laser-induced graphene (LIG) is obtained via a facile and cost-effective method that involves irradiation of a PI film with a laser to convert it into graphene [13]. Thus, LIG can be directly applied to flexible substrates, significantly enhancing their thermal characteristics by improving the thermal conductivity and wicking performance with the aid of their porous structures. Inagaki et al. reviewed the graphitization process of PI film [14]. PI is graphitized about 3000 °C. While it is hard to rapidly reach temperatures as high as 3000 °C using conventional methods, laser technology provides the necessary energy efficiently. Duy et al. conducted research on the graphene formation process based on laser power [15]. When the laser power is sufficient, polyimide undergoes graphitization, and outgassing of oxygen and nitrogen results in the formation of a porous structure.

Laser-induced graphene (LIG) exhibits excellent mechanical and electrical properties, along with a broad surface area due to its porous structure. As a result, there has been a significant amount of research in various applications such as sensors and supercapacitors. Mamleyev et al. conducted research on the use of laser pyrolysis with the introduction of nitrogen gas to develop a urea sensor, capable of detecting urea concentrations as low as 10^{-4} M [16]. Kim et al. created a densificated LIG supercapacitor through twice performed laser pyrolysis, achieving a capacitance of 19.8 mF cm^{-2} at a current density of 0.05 mA cm^{-2} [17]. In addition, subjecting graphene to oxygen treatment introduces functional groups, such as ether, epoxy, hydroxyl, and carbonyl, fostering hydrophilic interactions with DI-water through hydrogen bonding, resulting in further improvement in the liquid supply capability. In this study, we developed various hierarchical porous-patterned LIG structures to improve the wicking performance on a flexible substrate with the aim of enhancing thermal management. These patterns were fabricated by direct laser writing on a PI substrate with precise adjustments to the laser operating conditions, pattern spacing, and number of laser paths. Subsequently, we conducted a comprehensive analysis of the surface characteristics of various LIG samples, both before and after oxygen plasma treatment, to investigate their wettability and potential for high liquid supply capability. The wicking performance of the LIG samples was accurately assessed using capillary rate-of-rise tests.

2. Method

2.1 Fabrication of laser-induced graphene

Fig. 1 is a schematic of LIG fabrication. We used a commercial PI film (McMaster-Carr, t_{PIfilm} = 0.003") as the substrate. Initially, the PI film was cleaned using ultrasonic baths of acetone and isopropyl alcohol for 5 min each, followed by a rinse with DI-water. The PI film was then subjected to continuous CO_2 laser irradiation (Synrad, vi-30, maximum power: 30 W, wavelength: 10.6 μm, scanning speed: 200 mm/s, and frequency: 5 kHz) under ambient conditions. The laser power was modulated using an attenuator ranging from 9 to 23 W. All the samples were fabricated with an inline pattern, as shown in Fig. 1(b). The focal beam size of the laser was 125 μm; consequently, the laser spacing was set at 125 μm to ensure complete laser coverage. The side and front views of the optical microscope image are shown in Fig. 1(c). The fabricated LIG surfaces were then subjected to oxygen plasma treatment (FemtoScience, Cione 6, Pmax: 50 W) in the RF mode (radiofrequency glow discharged at 50 kHz) using 50 sccm of O_2 and 50 W of power for 20 s. This process was employed to render the surface hydrophilic using a method previously introduced through numerous DFT (density functional theory) calculations

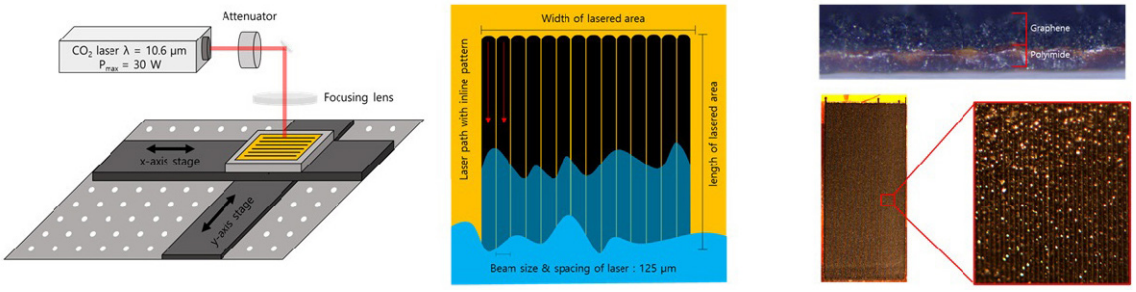

(a) (b) (c)

Fig. 1. Fabrication of patterned laser-induced graphene (LIG): (a) schematic of the fabrication setup; (b) exemplary depiction of LIG for wicking; (c) optical microscope image displaying LIG on a PI substrate.

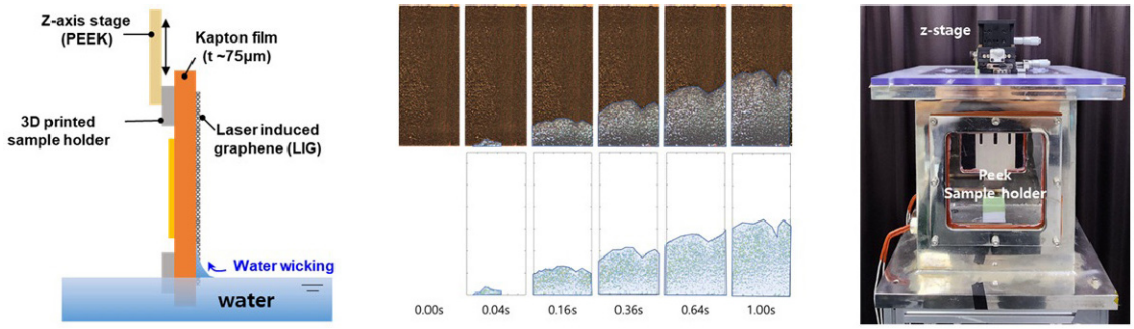

(a) (b) (c)

Fig. 2. Characterization of wicking performance: (a) schematic of the capillary rate-of-rise test; (b) image processing for quantifying average height variations; (c) photograph of the test chamber.

and experimental observation studies [18].

2.2 Characterization of wicking performance

The wicking performance was characterized by capillary rate-of-rise measurements. Fig. 2 shows a schematic of the experimental setup used to characterize the wicking performance. The samples were designed to be 10 mm wide and 20 mm high. They were secured onto a 3D printed sample holder made of clear resin (Formlabs, clear resin). The holder was mounted on a vertically adjustable PEEK stage situated within a chamber measuring 230 × 230 × 300 mm^3. The temperature and pressure were maintained at an ambient temperature of 18 °C and 1 atm, respectively, during measurement. The capillary rate-of-rise was recorded using a high-speed camera (Photron, FASTCAM Mini UX100, 500 fps) that captured the rise of the liquid through the LIG over time. MATLAB image processing was employed to delineate the surface boundary of the liquid, enabling a precise calculation of the wicking height. The parameters influencing the uncertainty of the wicking performance encompass high-speed imaging, time measurement, and height. For wicking speed measurement, the camera features a shutter speed of 3.9 μs and captures at 500 frames per second. The images have a resolution of 1280 × 1080 pixels, covering an area of 40 × 34 mm^2. Armed with this information, we incorporated error bars into Fig. 8.

3. Result and analysis

3.1 Surface analysis of laser-induced graphene

Fig. 3 shows the surface morphologies of various LIG samples captured using a field emission scanning electron microscope (FE-SEM, Carl Zeiss, model Sigma). Eight different samples were analyzed, each created with varying laser powers, starting from 9 W for case 1, and increasing by 2 W up to 23 W for case 8. Following the laser path, graphene nanowires were formed at the central location owing to laser ablation, followed by the creation of porous carbonaceous materials from PI via pyrolysis. Concurrently, graphene nanopores (highlighted in red in Fig. 3(a) emerged between the laser paths

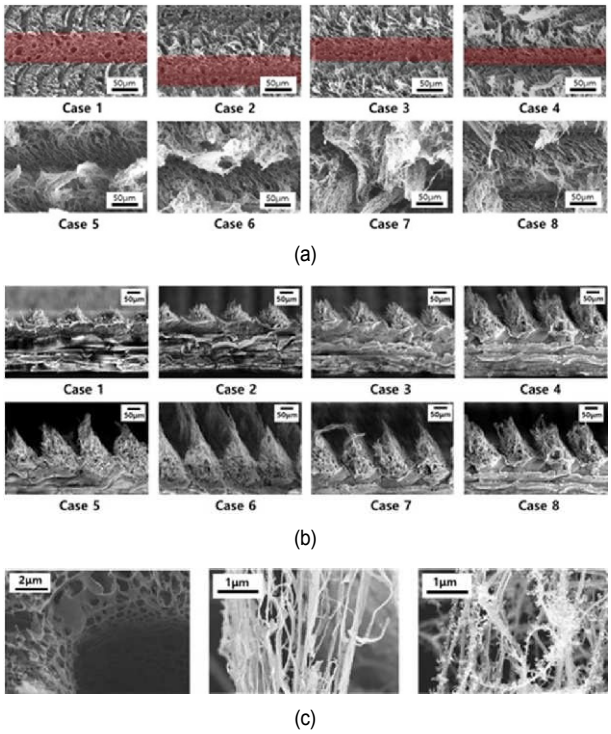

Fig. 3. FE-SEM images of LIG samples: (a) top view; (b) side view of samples; (c) enlarged images of graphene nanowires and nanopores. Cases 1-8 are fabricated using varying laser power, ranging from P_{laser} = 9 W for case 1 to P_{laser} = 23 W for case 8, with a 2 W increment. Enlarged images in (c) are obtained from P_{laser} = 13 W, 15 W, and 19 W.

owing to insufficient energy. These nanopores contained both large and small openings. As repetitive laser pulses accumulated heat, the molten PI began to boil and release gas, resulting in the formation of small pores on the surface [14, 15, 19]. These gases coalesced and were expelled, resulting in the formation of larger pores. Fig. 3(c) is an SEM image of a nanoporous structure, smooth nanowire structure, and graphene flake aggregated nanowire each. Nanoporous regions were clearly observed at relatively low laser powers of 9–15 W (cases 1–4). However, with increasing laser power, both the number and height of the nanowires increased, leading to a

Table 1. Specifications and experimental results of samples according to laser power.

	P_{laser} (W)	$t_{graphene}$ (μm)	$t_{PI\ film}$ (μm)
Case 1	9	62.7	56.2
Case 2	11	71.4	54.4
Case 3	13	81.9	51.1
Case 4	15	155.1	51.0
Case 5	17	163.9	45.0
Case 6	19	193.8	43.0
Case 7	21	228.8	38.2
Case 8	23	152.1	38.1

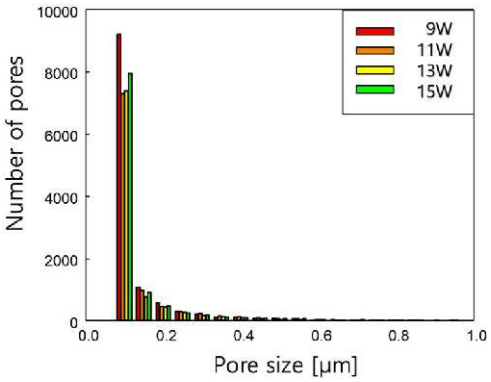

Fig. 4. The pore size distribution of LIG, which exhibited a dominant pore structure, was examined for laser power ranging from 9 W to 15 W.

decrease in the number of nanopores. Additionally, for higher powers $P_{laser} \geq 17$ W, nanowires aggregated with each other and formed clusters of graphene flakes on the stem of the nanowires. The sizes of both the nanowires and nanopores were evaluated by image analysis using ImageJ and averaged at ten different locations. The diameter of smooth nanowires reached up to d_{nw} = 1 μm. Aggregated nanowires had a diameter size similar to that of smooth wires. The size of graphene flakes differed. The thickness of the LIG was determined by measuring the side view of the FE-SEM image shown in Fig. 3(b); this measurement was averaged at five different points. For laser powers up to 19 W (case 6), the height of the LIG pillar showed an increasing trend within the range of 63–229 μm as the laser power increased. However, for powers higher than 19 W, the height remained almost consistent or was slightly smaller at 23 W, probably owing to the strong laser causing the aggregated bunches of graphene to disperse. The comprehensive laser parameters, along with the thicknesses of the graphene and PI films for each sample, are listed in Table 1.

Fig. 4 presents the pore distribution of LIG for laser power ranging from 9 W to 15 W. The large pores ranged in size from 1–10 μm, and the small pores ranged in size from 10–100 nm. The pore distribution indicated that pores with d_{pore} = 30–50 nm constituted 50 % of the total, and pores with d_{pore} = 50–100 nm constituted 25 % of the total. As the laser power increases,

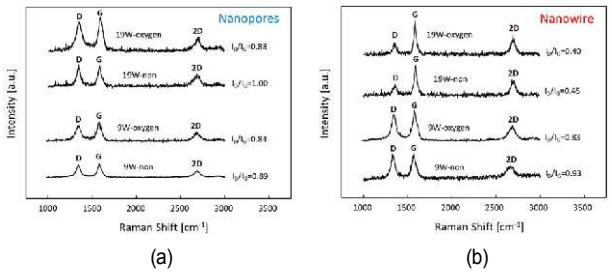

(a) (b)

Fig. 5. Raman spectra results of LIGs. Samples are fabricated using laser powers of 9 W and 19 W and I_D/I_G are compared in the region of (a) nanopores; (b) nanowires.

there is a tendency for the number of pores in the range of 30-50 nm to increase, while the number of larger pores decreases. The reason for this is that as the laser power increases, the porous structure transforms into a nanowire structure, leading to an overall decrease in the number of pores.

Fig. 5 presents the Raman spectra results obtained from two distinct LIGs fabricated at P_{laser} values of 9 and 19 W, focusing on the areas near the nanopores and nanowires. The measurements were conducted with a λ_{laser} of 532 nm, encompassing a range of Raman shift from 1000 cm^{-1} to 3000 cm^{-1}. The laser power was maintained at 5 mW to prevent laser-induced damage. All measurements were at room temperature of 22 °C, and the values were obtained as the average of five random point measurements. The Raman spectrum of graphene primarily exhibited peaks at D (1350 cm^{-1}), G (1580 cm^{-1}), and 2D (2700 cm^{-1}). The D peak resulted from defects or bent sp^2 carbon bonds in graphene, whereas the G peak resulted from the in-plane vibrations of sp^2 carbon atoms, collectively reflecting the characteristics of amorphous and graphitic carbon in LIG, respectively. The intensity ratio of I_D/I_G, where I_D is the intensity of the D peak and I_G is the intensity of the G peak, serves as a parameter for assessing the defect density in graphene; a smaller value of this parameter indicates a higher prevalence of a graphene-like structure [20]. For the LIG samples with a relatively low laser power of 9 W, both the nanopores and nanowires exhibited an I_D/I_G ratio of approximately 0.9. This suggests that the LIG did not fully transition into a nanowire structure, probably because the laser irradiation temperature did not reach an adequate level of carbonization. At a higher laser power of 19 W, the nanowire exhibited an I_D/I_G of 0.45, indicating a relatively more graphene-like structure, whereas I_D/I_G still showed high values near the nanopore areas. As the laser power increased, more energy was delivered to the PI film, leading to a high degree of graphene formation and a nanowire structure. And, after treating oxygen plasma, overall I_D/I_G ratios tend to be reduced about 0.05 ~ 0.1. This is because after oxygen plasma treatment, oxygen connected at carbon defect.

Fig. 6(a) shows the X-ray diffraction (XRD, Bruker-AXS, New D8-Advance, Cu kα) results of the LIG both before and after oxygen plasma treatment. The prominent peak at 2θ = 26.4°, corresponding to (002), validated the existence of graphene,

with an interlayer spacing (d-spacing, d) calculated at 3.37 Å using the Bragg's law. The inset image obtained from field emission-transmission electron microscopy (FE-TEM, JEOL, JEM-F200) provides additional confirmation of the graphene structure with interlayer spacing consistent with previous studies [14, 16, 17, 21, 22]. Following oxygen plasma treatment, additional peaks at 2θ = 21.6° and 24.0° emerged, that were absent in the before-plasma LIG sample, indicating the presence of oxidized graphene. These peaks suggest an increase in interlayer spacing to 3.4 Å and 4.1 Å, respectively, attributed to the introduction of ether groups, as shown in the XPS result in Figs. 6(c) and (d). Xu et al. reported that the attachment of oxygen to graphene in the form of ether functional groups induces polarity, leading to hydrophilicity [19]. Figs. 6(b)-(d) show X-ray photoelectron spectra (XPS, Thermo Fisher, Scientific K-Alpha+) before and after oxygen plasma treatment. Fig. 6(b) shows the changes in the atomic ratios with the oxygen plasma treatment. In the before-plasma LIG sample, the composition was C = 97.3 % and O = 2.7 %, that changed to C = 86.8 % and O = 12.2 %, indicating an increased oxygen content after the oxygen plasma treatment. As shown in Figs. 6(c) and (d), the C1s spectrum demonstrated that most of the bonds were in the form of C-O after the oxygen plasma treatment, whereas non-oxidized graphene primarily exhibited C-C sp^2 bonding with minor oxygen states before the plasma treatment. The increased surface oxygen content in the oxygen plasma-treated sample contributed to its enhanced hydrophilicity.

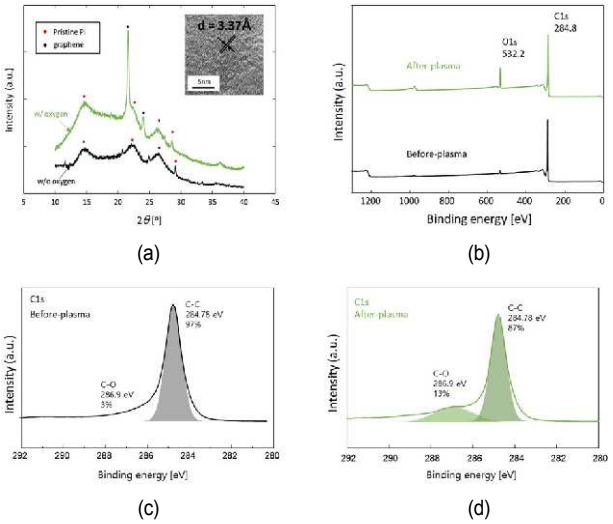

Fig. 6. X-ray diffraction (XRD) and X-ray photoelectron spectra (XPS) of the LIG before and after oxygen treatment: (a) the XRD of the LIG before and after oxygen treatment; (b) XPS survey of the LIG before and after oxygen treatment; (c) and (d) C1s of the LIG before and after oxygen treatment.

3.2 Characterization of wicking performance

Fig. 7 shows the results of the capillary rate-of-rise measurements for various LIG samples produced at different laser power levels, ranging from P_{laser} = 9 W for case 1 to P_{laser} = 23 W for case 8, with a 2-W increment. The capillary rate-of-rise appears relatively slow for samples with lower laser powers of 9 and 11 W. However, with increasing laser power, the capillary rate-of-rise noticeably increased. Notably, the laser power of P_{laser} = 23 W exhibited a comparable rate to that observed at P_{laser} = 17 and 19 W. This trend corresponded to the height of the LIG nanowire pillars. As the laser power increased, both the number of bundles and the height of the graphene nanowires increased. This resulted in a larger contact area between the liquid and graphene, facilitating faster liquid delivery. The height of the nanowires continued to increase until case 7 (P_{laser} = 21 W). This led to the maximum capillary rate-of-rise observed in case 7. We observed shorter nanowires in case 8, as shown in Fig. 3, because the high laser power caused the graphene to blast away, resulting in a decrease in the capillary rate-of-rise. The nanoporous structures created with lower laser powers (cases 1–3) had smaller contact areas than the samples dominated by nanowires, leading to a slower liquid transport speed. Fig. 8 illustrates the characteristics of the wicking performance across all the LIG samples. The x-axis represents the square root of time, that is used to calculate

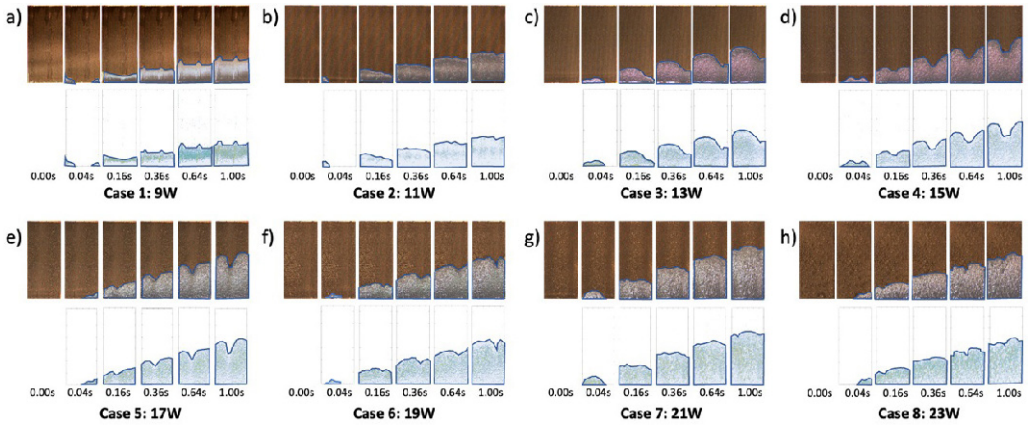

Fig. 7. Results of capillary rise rate measurements: (a)-(h) height variations over time for different LIG samples fabricated at P_{laser} levels, ranging from P_{laser} = 9 W for case 1 to P_{laser} = 23 W for case 8, with a 2-W increment.

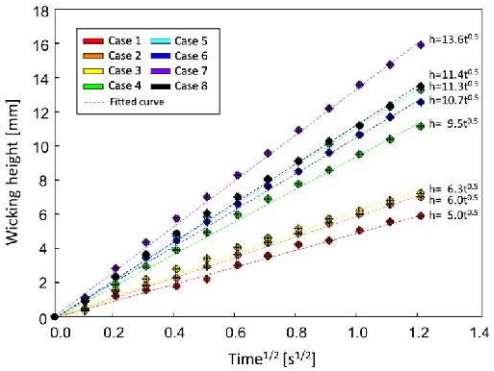

Fig. 8. Results of the capillary rate-of-rise measurement for LIGs produced at various laser powers.

the wicking velocity based on the Lucas–Washburn equation [23], which expresses the relationship between the wicking height and time. As indicated in the results, cases 1–3, produced with a lower laser power, exhibit a lower wicking performance, primarily owing to the prevalence of nanopore structures. The wicking performance increased with increasing laser power. A significant improvement in the wicking performance was observed at relatively high laser powers (P_{laser} > 15 W); this was attributed to the formation of thicker and taller nanowires. The maximum wicking performance was achieved at a laser power of 21 W (case 7), demonstrating a nearly three-fold increase in the liquid transport speed compared with that observed at 9 W (case 1).

The wicking velocities derived from the wicking performance results are shown in Fig. 9(a). The wicking velocity was determined through curve fitting, employing the slope value from the wicking height versus the square root of time plot, with an R-value of $\geq$ 0.99. The wicking velocities from eight distinct LIG samples exhibited a range from 5.0 to 13.6 mm/s$^{0.5}$, with the slowest observed at the lowest laser power of 9 W, and the fastest at a laser power of 21 W. In cases where nanopores were prevalent in the LIG, such as cases 1–3, the wicking velocities displayed a relatively modest range, falling between 5.0 and 6.3 mm/s$^{0.5}$. However, with increasing laser power, wicking velocities experienced a substantial increase, ranging from 9.5 to 13.6 mm/s$^{0.5}$, aided by an increase in liquid delivery owing to the appearance of nanowires. Fig. 9(b) shows a benchmark comparison of the wicking velocities obtained from relevant existing studies in literature. Because no literature is available on the wicking performance in a flexible substrate, we compared the results from a solid substrate. Yuan et al. [12] determined the wicking velocities using droplet spreading measurements, whereas all other studies, including the present study, employed the capillary rate-of-rise method. Because the droplet spreading measurement neglects the gravitational effect, its wicking velocity can be overpredicted compared with the capillary rate-of-rise measurement, particularly for relatively large droplet sizes.

As demonstrated in Fig. 9, the LIG produced in the present study exhibited the highest wicking velocity compared with

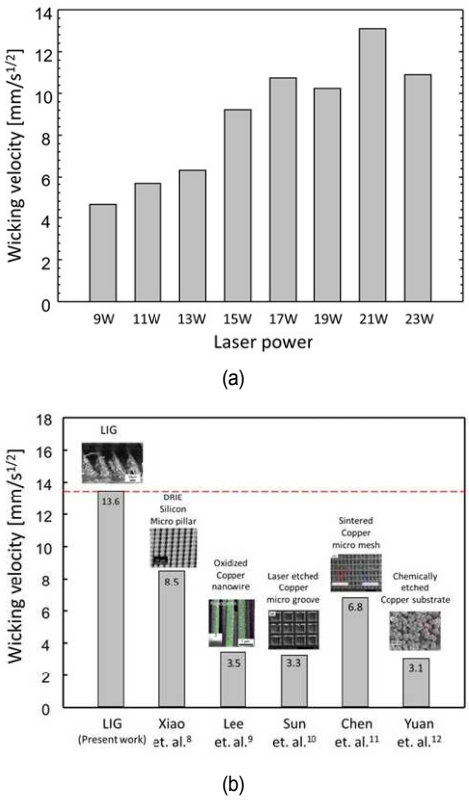

Fig. 9. Characterization of the wicking velocity in the LIG: (a) wicking velocity of LIGs at various laser power levels; (b) comparative analysis of the wicking velocity benchmarked against pertinent prior studies.

other benchmark samples examined in relevant studies. The surface of the LIG demonstrated a nearly fourfold improvement in wicking velocity in contrast to copper nanowire [9], laser etched copper micro groove [10], and chemically etched copper substrate [12]. Furthermore, it showed an even greater wicking velocity, approximately 63 % and 50 % faster than those of the Si DRIE micropillar [8] and Cu wire mesh [11]. Except for the current study, Si micropillar [8] exhibited the best performance in wicking velocity, although it registered a speed of 8.5 mm/s$^{0.5}$; this speed was approximately 37 % slower than that in the present study.

4. Conclusions

We devised a range of intricate porous patterns on graphene structures to enhance the wicking performance on a flexible substrate. These patterns were created through direct laser writing, utilizing a CO_2 laser on a PI substrate, with specific parameters: a laser scanning speed of 200 mm/s, frequency of 5 kHz, and laser spacing of 125 μm. We compared eight distinct LIG samples, each with different laser powers varying from 9 to 23 W in 2-W increments. A thorough surface analysis via FE-SEM and Raman spectroscopy verified the successful formation of porous carbonaceous materials from PI, leading to the creation of porous graphene through laser ablation. We observed that two distinct types of porous graphene were pro-

duced in LIG: nanopore structures were predominantly observed at relatively lower power levels ($P_{laser} \leq 13$ W), whereas nanowires were primarily generated at higher laser powers ($P_{laser} \geq 15$ W). As the laser power increased, both the quantity and height of nanowires increased, resulting in a reduction in the nanopore area. An indepth examination of the surface properties was performed both before and after the oxygen plasma treatment, utilizing 50 sccm of O_2 and 50 W of power for 20 s. The XRD and XPS results confirmed that the application of the oxygen plasma treatment expanded the interlayer spacing of graphene and elevated the oxygen content on the surface, thereby enhancing its hydrophilicity.

The liquid transport capability of the LIG samples was precisely measured using the capillary rate-of-rise method. Lower laser powers (9 and 11 W) showed a slow increase, whereas higher powers showed a rapid increase. A higher laser power led to taller nanowires, enhancing the liquid contact and delivery speed. The nanowire height peaked at P_{laser} = 21 W, yielding the highest rise rate and P_{laser} = 23 W resulted in shorter nanowires owing to graphene aggregation from the strong laser power, thereby reducing the rise rate. Nanoporous structures with lower laser powers had smaller contacts, resulting in slower liquid transport. Wicking velocity was also compared for eight LIG samples ranging from 5.0 to 13.6 mm/s$^{0.5}$, with the slowest at 9 W and the fastest at 21 W. In cases dominated by nanopores with relatively low laser powers of 9–13 W, the wicking velocity ranged from 5.0 to 6.3 mm/s$^{0.5}$. Higher laser power led to significant increases, reaching 9.5 to 13.6 mm/s$^{0.5}$ for $P_{laser} \geq 15$ W owing to the emergence of nanowires. The wicking velocity in the current study was assessed in relation to the data from pertinent prior studies. Notably, the LIG displayed the highest wicking velocity among the benchmark samples investigated in relevant studies, particularly achieving up to four times the velocity of existing porous structures.

Acknowledgments

This research was supported by the Challengeable Future Defense Technology Research and Development Program through the Agency For Defense Development (ADD) funded by the Defense Acquisition Program Administration (DAPA) in 2022 (No.915027201), and the Chung-Ang University Graduate Research Scholarship in 2023.

References

[1] E. W. Zaia, M. P. Gordon, P. Yuan and J. J. Urban, Progress and perspective: soft thermoelectric materials for wearable and internet‐of‐things applications, *Adv. Electron. Mater.*, 5 (11) (2019) 1800823.

[2] A. Sadeghi-Niaraki, Internet of thing (IoT) review of review: Bibliometric overview since its foundation, *Future Generation Computer Systems*, 143 (2023) 361-377.

[3] Y. Jiuhong and Y. Xianyu, Gold nanomaterials‐implemented wearable sensors for healthcare applications, *Advanced Functional Materials*, 32 (19) (2022) 2113012.

[4] R. Li, M. Panahi-Sarmad, T. Chen, A. Wang, R. Xu and X. Xiao, Highly sensitive and flexible capacitive pressure sensor based on a dual-structured nanofiber membrane as the dielectric for attachable wearable electronics, *ACS Appl. Electron. Mater.*, 4 (1) (2022) 469-477.

[5] C. Li, H. Chen, S. Zhang, W. Yang, M. Gao, P. Huang, M. Wu, Z. Sun, J. Wang and X. Wei, Wearable and biocompatible blood oxygen sensor based on heterogeneously integrated lasers on a laser-induced graphene electrode, *ACS Appl. Electron. Mater.*, 4 (4) (2022) 1583-1591.

[6] R. Bahru, A. A. Hamzah and M. A. Mohamed, Thermal management of wearable and implantable electronic healthcare devices: perspective and measurement approach, *Int. J. Energy Res.*, 45 (2) (2021) 1517-1534.

[7] Y. Jung, I. Ha, M. Kim, J. Ahn, J. Lee and S. H. Ko, High heat storing and thermally diffusive artificial skin for wearable thermal management, *Nano Energy*, 105 (2023) 107979.

[8] R. Xiao, R. Enright and E. N. Wang, Prediction and optimization of liquid propagation in micropillar arrays, *Langmuir*, 26 (19) (2010) 15070-15075.

[9] J. Lee, Y. Suh, P. P. Dubey, M. T. Barako and Y. Won, Capillary wicking in hierarchically textured copper nanowire arrays, *ACS Appl. Mater. Interfaces*, 11 (1) (2019) 1546-1554.

[10] Y. Sun, M. Shuai, S. Zhang, Y. Tang, G. Chen and G. Zhong, Hierarchically 3D-textured copper surfaces with enhanced wicking properties for high-power cooling, *Applied Thermal Engineering*, 178 (2020) 115650.

[11] G. Chen, D. Fan, S. Zhang, Y. Sun, G. Zhong, Z. Wang, Z. Wan and Y. Tang, Wicking capability evaluation of multilayer composite micromesh wicks for ultrathin two-phase heat transfer devices, *Renewable Energy*, 163 (2021) 921-929.

[12] X. Yuan, Y. Du, G. Fei, R. Yang, C. Wang, Q. Xu and C. Li, Experimental study on developing in-situ hierarchical micro/nanocrystals for improved capillary wicking, *Microfluid Nanofluid*, 27 (2023) 31.

[13] J. Lin, Z. Peng, Y. Liu, F. Ruiz-Zepeda, R. Ye, E. L. G. Samuel, M. J. Yacaman, B. I. Yakobson and J. M. Tour, Laser-induced porous graphene films from commercial polymers, *Nature Communications*, 5 (2014) 5714.

[14] M. Inagaki, N. Ohta and Y. Hishiyama, Aromatic polyimides as carbon precursors, *Carbon*, 61 (2013) 1-21.

[15] L. X. Duy, Z. Peng, J. Zhang, Y. Ji and J. M. Tour, Laser-induced graphene fibers, *Carbon*, 126 (2018) 472-479.

[16] E. R. Mamleyev, S. Heissler, A. Nefedov, P. G. Weidler, N. Nordin, V. V. Kudryashov, K. Lange, N. MacKinnon and S. Sharma, Laser-induced hierarchical carbon patterns on polyimide substrates for flexible urea sensors, *Npj Flex Electron*, 3 (1) (2019) 2.

[17] K. Y. Kim, H. Choi, C. V. Tran and J. B. In, Simultaneous densification and nitrogen doping of laser-induced graphene by duplicated pyrolysis for supercapacitor applications, *J. of Power Sources*, 441 (2019) 227199.

[18] Z. Xu, Z. Ao, D. Chu, A. Younis, C. M. Li and S. Li, Reversible hydrophobic to hydrophilic transition in graphene via water

splitting induced by UV irradiation, *Sci. Rep.*, 4 (1) (2015) 6450.
[19] R. Ye, D. K. James and J. M. Tour, Laser-induced graphene, *Acc. Chem. Res.*, 51 (7) (2018) 1609-1620.
[20] A. C. Ferrari, J. C. Meyer, V. Scardaci, C. Casiraghi, M. Lazzeri, F. Mauri, S. Piscanec, D. Jiang, K. S. Novoselov, S. Roth and A. K. Geim, Raman spectrum of graphene and graphene layers, *Phys. Rev. Lett.*, 97 (18) (2006) 187401.
[21] D. Kong, M. Kang, K. Y. Kim, J. Jang, J. Cho and J. B. In, Hierarchically structured laser-induced graphene for enhanced boiling on flexible substrates, *ACS Appl. Mater. Interfaces*, 12 (33) (2020) 37784-37792.
[22] H. C. Shim, C. V. Tran, S. Hyun and J. B. In, Three-dimensional laser-induced holey graphene and its dry release transfer onto Cu foil for high-rate energy storage in lithium-ion batteries, *Applied Surface Science*, 564 (2021) 150416.
[23] N. Fries and M. Dreyer, An analytic solution of capillary rise restrained by gravity, *J. of Colloid and Interface Science*, 320 (1) (2008) 259-263.

Minsoo Kang received a B.S. in Mechanical Engineering from Chung-Ang University, in 2020. He is now pursuing his integrated Ph. D. in the Department of Intelligent Energy and Industry, Chung-Ang University. His main research interests are enhancing the performance and efficiency of semiconductor devices by effectively managing high heat flux.

Daeyoung Kong received Ph.D. from the Department of Intelligent Energy and Industry from Chung-Ang University, South Korea in 2023. Since 2023, he's worked consistently in the Nanoheat group at Stanford University as a visiting postdoctoral scholar. His specialized studies focus on the development of advanced microfluidic coolers for the application of extremely high heat flux electronics.

Junrae Park received a B.S. in Mechanical Engineering from Chung-Ang University, in 2023. He is now pursuing his integrated M.S. in the Department of Intelligent Energy and Industry, Chung-Ang University. His main research interests are micro-scale cooling systems for high power semiconductor devices.

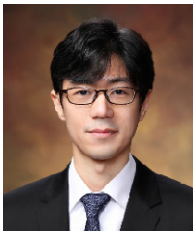

Jung Bin In is currently a Professor of Mechanical Engineering, Chung-Ang University, Seoul, South Korea. He received the Ph.D. in Mechanical Engineering from the University of California, Berkeley, CA, USA, in 2011. His research interests include micro-cooling devices, laser processing, and laser-based additive manufacturing.

Hyoungsoon Lee is an Associate Professor of Mechanical Engineering, Chung-Ang University, Seoul, Korea. He received his B.S. (2006) in Mechanical Engineering from Korea University, Seoul, Korea, and completed his M.S. (2011) and Ph.D. (2014) in Mechanical Engineering from Purdue University. His research interests include phase change heat transfer, thermal management in electronics.